

Topological Descendants of Multicritical EuTl_2

Lin-Lin Wang¹, Hoi Chun Po², Robert-Jan Slager^{3,4}, and Ashvin Vishwanath⁴

¹Ames Laboratory, U.S. Department of Energy, Ames, IA 50011, USA

²Department of Physics, Massachusetts Institute of Technology, Cambridge, MA 02139,
USA

³TCM Group, Cavendish Laboratory, University of Cambridge, J. J. Thomson Avenue,
Cambridge CB3 0HE, United Kingdom

⁴Department of Physics, Harvard University, Cambridge, MA 02138, USA

Abstract

The past decades have witnessed a transformation in characterizing condensed matter systems with topology. Aided by a refined understanding of topological band structures with crystalline symmetries that has emerged recently, many electronic phases have been identified and a plethora of materials have been predicted to host novel properties and functionalities. A key underlying question, also with respect to future application, is to what extent the related physical features can be manipulated, especially in the context of magnetic order. Here we describe a paradigmatic semimetal that simultaneously incorporates multiple, and sometimes conflicting topology which guarantees gaplessness and leads to an exceptionally rich family of descendent phases on lowering symmetry. We predict that this multicritical phase is realized in EuTl_2 . Starting from the parent semimetallic state, which already separates two topological insulating regimes, the interplay of inherent magnetism and strain allows for an exceptionally rich phase diagram of topological descendant states.

Introduction

An important outstanding question in the field of topological materials¹⁻⁴ is how their robust physical properties, such as anomalous surface states and quantized responses, could be leveraged for technological applications. Combining nontrivial electronic topology⁵⁻¹³ with magnetism¹⁴ provides a promising route forward, with the prospect that the presence or absence of certain robust responses could be tuned dynamically through an external magnetic field. Such sensitivity of topological character on magnetism, however, is not always guaranteed in a magnetic topological material. For example, a magnetic axion insulator protected by inversion symmetry¹⁵⁻¹⁷ could be viewed as the natural continuation of a parent paramagnetic or nonmagnetic strong topological insulator (TI), in the sense that no bulk band gap closing is required in going between the two phases. This is the case in the recently discovered anti-ferromagnetic (AFM) TI in the $\text{MnBi}_2\text{Te}_4(\text{Bi}_2\text{Te}_3)_m$ series¹⁸⁻²⁴ and the predicted AFM higher-order TI and topological crystalline insulator (TCI) in EuIn_2As_2 ²⁵.

A natural paradigm for discovering materials with the desired strong interplay between magnetism and electronic topology is to focus on semimetallic parent phases with time-reversal symmetry (TRS) which are symmetry-tuned to a multicritical point between different topological phases. If such a phase is realized in a compound with an innate magnetic instability, then different topological phases could be naturally spawned in conjunction with different magnetic orders. In this work, we theoretically propose EuTi_2 as a prototype candidate for this paradigm. In the parent phase, the system is a Dirac semimetal (DSM) whose gaplessness could be attributed to the competition between the opposing tendency to realizing a strong TI and a TCI. A plethora of distinct topological phases descends from this parent phase upon the breaking of symmetries either by strain or by the development of magnetic orders as summarized in Fig.1. In particular, the set of daughter phases include (i) paramagnetic TCIs protected by different spatial symmetries with two sets of mirror Chern numbers (MCN), (ii) AFM Dirac semimetal (AFM-DSM), (iii) AFM axion insulator, and (iv) ferromagnetic (FM) Weyl semimetal (FM-WSM). The set of topological phases realizable in this system are summarized in Table 1 together with their associated space groups, magnetic space groups and the relevant topological indices.

Results and Discussion

Magnetic topological phases from a multicritical parent

We begin by elaborating on how a multicritical parent phase with TRS could serve as a promising starting point for the search for topological magnetic phases. Topologically nontrivial insulators come in two varieties: Chern insulators like that realized in the Haldane model²⁶ and anomalous quantum Hall effect²⁷ do not require symmetry protection, whereas phases like the quantum spin-Hall insulator and TCIs require protecting symmetries, e.g. TRS and crystalline symmetries. In some systems the nontrivial ground state could be simultaneously protected by multiple symmetries. A common example concerns centrosymmetric three-dimensional strong TI with significant spin-orbit coupling (SOC) and TRS. The nontrivial magnetoelectric response is quantized provided at least one of spatial inversion and time-reversal symmetries is preserved. As such, if inversion-preserving magnetism is induced in the strong TI, one naturally arrives at a magnetic TI which is dubbed an “axion insulator.” This design strategy has led to the discovery of magnetic TIs in the $\text{MnBi}_2\text{Te}_4(\text{Bi}_2\text{Te}_3)_m$ series¹⁸⁻²⁴.

A corresponding dichotomy on the stability of topological semimetal (TSM) with respect to symmetry breaking could also be advanced for TSMs: while 3D WSMs are stable for a finite range of system parameters, the 3D DSM requires symmetry protection, and as such could be gapped out by an infinitesimal symmetry-breaking perturbation. However, there is an important distinction in the semimetallic case, since generically distinct gapped phases could be realized by the symmetry lowering. Equivalently, symmetry-protected TSMs could be viewed as being pinned to a critical point between topologically distinct phases. Indeed, it is known that the 3D DSMs can be viewed as a critical point between phases with different strong and weak Z_2 indices, and these phases could be accessed by applying suitable strains to the crystal²⁸. The TSM could even be multicritical, in the sense that more than two descendent topological phases could be realized with different symmetry breaking patterns. This is especially true in the presence of crystalline symmetries, which leads to a rich set of topological phases mirroring the corresponding richness of spatial symmetry patterns in crystals⁹. Consequently, TSMs inherently have a richer phase diagram as a function of symmetry-lowering perturbations. That is, they could

remain stable, be converted into a different variety of TSM (e.g. splitting a Dirac point to Weyl points), or become distinct gapped topological phases depending on the sign of the perturbation. As a concrete example, let us turn to the phases realizable in EuTl_2 , which is a DSM protected by the 3-fold rotation symmetry (C_3) in the paramagnetic phase. The spatial symmetries include two sets of mirror planes which are respectively horizontal or vertical, and as such we could define MCNs for each of the planes. However, the Dirac points lie on the C_3 rotation axis and render the vertical MCN ill-defined. Correspondingly, upon lattice distortion with strain to remove C_3 and gap out the Dirac points, the horizontal MCN remains unchanged but the vertical MCN becomes either 2 or 0, depending on the sign (i.e., tensile vs. compressive) of the strain. This shows explicitly how changing the sign of the strain could result in different TCI phases.

There are, however, three main drawbacks in using strain as an experimental knob to access the phase diagram around a symmetry-protected TSMs: first, the crystal symmetries may conspire to leave only a single natural straining direction, making it impossible to access some of the descendant phases of the parent multicritical TSM. Second, tensile strain is generally harder to sustain than compressive strain in a crystal, which means it may not be physically feasible to access both sides of the phase diagram. Finally, the attainable strain level in a crystal is usually small (at a few %), and, unless the system is close to a structural instability, this translates into a quantitatively small effect on the electronic properties.

The incorporation of magnetism into the problem provides an important new route, as its richness and spontaneous nature provide access to a much larger phase space starting from a multicritical parent TSM. In addition, for systems with competing magnetic states it may be possible to select different magnetic orders by changing growth conditions, as recently shown for EuCd_2As_2 in experiment, where both AFM and FM samples²⁹ can be grown. The according control is one of the most important outstanding challenges in converting electronic topology into topological electronics. As such, searching for a multicritical TSM parent with magnetic descendant topological phases could be a useful guiding principle in functionalizing topological materials. For EuTl_2 (Fig.1), different magnetic configurations can give a range of different topological phases, which are also summarized in Table 1. Below we will discuss these topological phases in EuTl_2 with

details, and show that the multicritical behavior indeed results in a myriad of phases. Such abundance of descendent topological phases stands in rather stark contrast with the stable gapped AFM order in, e.g., the $\text{MnBi}_2\text{Te}_4(\text{Bi}_2\text{Te}_3)_m$ ¹⁸⁻²⁴.

EuTl₂ as a case example of a multicritical parent

The crystal structure of EuTl₂ (Fig.2(a)) in space group 194 (P6₃/mmc) has two oppositely buckled honeycomb Tl layers and both are sandwiched between two hexagonal Eu layers. The space group symmetry generators are the inversion P , 3-fold rotation C_3 , 2-fold screw S_2 along the c -axis, and 2-fold rotation along the a or b -axis, labelled as $C_{2;[010]}$ or C_{2y} . With the Cartesian coordinate system chosen for y (z) along b (c)-axis, the Miller index of $[\bar{1}\bar{2}10]$ and $[10\bar{1}0]$ in hexagonal coordinate is equivalent to $[010]$ and $[100]$ in Cartesian coordinates, respectively. The 6-fold screw along the c -axis, S_6 , is composed of C_3 and S_2 . There is a mirror symmetry, labeled as $M_{(001)}$ or M_z , about the horizontal plane normal to the c -axis. Similarly, the symmetries about another set of vertical mirror planes normal to the a or b -axis are labeled as $M_{(010)}$ or M_y . There are also vertical glide planes $G_{(100)}$ or G_x , spanned by c -axis and a or b -axis, and we denote the 2-fold rotation about the normal of the glide plane by $C_{2;[100]}$ or C_{2x} . The inversion center locates at the midpoint of the Tl-Tl bond in the buckled honeycomb layer. Figure 2(b) shows the 3D bulk Brillouin zone (BZ) of EuTl₂ and the 2D surface Brillouin zone (SBZ) for the (001) and (010) surfaces with high-symmetry points labeled.

The bulk band structures calculated with PBE+SOC is plotted in Fig.2(c) for nonmagnetic EuTl₂, where the half-filled Eu 4f orbitals are treated as core states. There is a continuous gap between the top valence and bottom conduction bands except for the crossing point along the Γ -A direction. The band dispersion near the crossing point, zoomed in Fig.2(d), shows that the gap vanishes in conjunction with a change in orbital projection of Tl p_y . Note that there is a near degeneracy along the Γ -K line but a small gap is sustained. As such, we conclude the most important degrees of freedom near the Fermi energy (E_F) is the pair of bulk Dirac points (BDPs) at momentum-energy $(0.0, 0.0, \pm 0.36 \text{ \AA}^{-1}; E_F - 0.19 \text{ eV})$. On one hand, the BDPs are protected by C_3 , since the states crossing at the BDP have distinct C_3 eigenvalues. On the other hand, the parity eigenvalues at time-

reversal invariant momentum (TRIM) gives a nontrivial Z_4 -valued symmetry indicator of 2, indicating the system could be viewed as a would-be TCI if not for the presence of the BDPs. Because the gaplessness is only along the Γ - A direction, the M_z MCN^{30, 31} on the $k_z=0$ and π planes are well-defined and calculated as 2 and 0, respectively, from the Wannier charge center (WCC) evolution (see Fig.S1 in SI).

We now address how the topological features in the bulk manifest on the surfaces. From the surface states on (001) in Fig.2(e), there are surface Dirac points (SDPs) at the three TRIM points, \bar{M} . Such SDPs should be protected by M_y symmetry. But the M_y MCN cannot be calculated because of the gaplessness along the Γ - A direction on the $k_y=0$ plane. As zoomed along \bar{K} - $\bar{\Gamma}$ - \bar{M} direction in Fig.2(g), surface states converging to the BDP projection on (001). Together with the three SDPs at \bar{M} , there are four gapless points on (001). In Fig.2(f), we also show the surface state spectrum on the (010). As the glide symmetry is preserved, the surface states along the \bar{X} - \bar{S} - \bar{Y} direction correspond to that of the hourglass³² fermions. The double degeneracy of surface state along \bar{S} - \bar{Y} is protected by TG_x and the hourglass crossing (zoomed in Fig.2(h)) is protected by G_x . All in all, we find that the bulk and surface band structures of EuTl₂ showcase three types of topological features protected by different symmetries, namely, bulk Dirac point, surface Dirac points and hourglass fermions.

Descendent states under strain

As a next step, we consider the topological phases descending from the high-symmetry parent phase characterized above. We will first consider in details the effects of a uniaxial strain along the hexagonal $[1\bar{1}00]$ direction, which breaks the C_3 symmetry to create an insulating phase by gapping out the BDP along the Γ - A direction, while preserving every other symmetry element (see Table 1). The space group is changed from 194 to 63. This analysis will then serve as the foundation upon which we can readily understand the topological characters of the various magnetic phases. As shown in Fig.3(a), with a -2% strain, a 6 meV gap is opened at the innate BDP. Correspondingly, on the (001) a gap opens up in the projection of the bulk bands and a SDP emerges (Fig. 3(b)). As the SDPs at the other three TRIM are unaffected by the perturbation (Fig.3(d)), we see that the system has an even number of SDPs and is therefore not a strong TI, in distinct contrast to

BaHgSn³³ and KAuTe³⁴. This still leaves the possibility that EuTl₂ under strain is a TCI. To investigate this, we compute the M_y MCN, which is now well-defined with the BDP being gapped out. The calculated M_y MCN is 2 and 0 for -2% and $+2\%$ strain, respectively, as shown in Fig.3(c) and (e). Together with the unchanged M_z MCN of 2, this certifies that the system is a TCI at least for compressive strain. Furthermore, if one views the undistorted phase as a critical point between the two classes of strained structures, then it would be natural to assign M_y MCN=1 to the high-symmetry parent phase despite the BDPs render the M_y MCN ill-defined in a strict sense. This picture helps to elucidate on the gaplessness of the system: on the one hand, from considerations of both the symmetry indicators and the M_z MCNs, we see that the system is not a strong TI; on the other hand, the natural M_y MCN assignment to the undistorted phase is only consistent with a strong TI. The presence of the BDPs could then be viewed as the resolution between the contradictions derived from considering different sets of spatial symmetries.

We characterize the nature of the TCI realized in EuTl₂ with tensile strain. The strain does not break the M_z or G_x symmetries, and the small perturbation has little effect on the Bloch states on the $k_z=0$ and π planes. As such, the M_z MCN of 2 and 0 on these planes for the higher-symmetry structure survives for both compressive and tensile strain. In fact, the topological characters of an insulator with respect to multiple crystalline symmetries are intertwined^{9, 10, 35, 36}, and based on the MCNs for M_y and M_z we have computed, one can infer the TCI indices associated with the other crystalline symmetries. The results are summarized in Table 1, and we see that EuTl₂ realizes distinct composite TCI phases depending on the nature of the strain.

Inspecting the surface state signatures, however, reveals a conundrum. As one can see in Fig.3(f) and (d), energetically the surface band structures on the (001), which preserves M_y , are almost identical for the tensile and compressive strains despite the system is respectively trivial and nontrivial as a M_y -protected TCI. Such surface behavior is nevertheless consistent with the bulk diagnosis: on a mirror-respecting surface, one could define a Z -valued topological invariant to each of the SDPs³⁰, and the defining feature of the anomalous surface of a nontrivial TCI bulk is that the total charge (even number) of SDPs is nonzero. Since the SDPs are all pinned to the TRIM points, the topological

distinction between the surface states with opposite strain cannot be discerned from the energetics alone, i.e., simply noting the distribution of the SDPs in the surface Brillouin zone does not allow one to uniquely determine the topological index of the system. Instead, one has to analyze the system from the bulk perspective, as we have done here, or evaluate the mirror-protected Z -valued topological invariants for each of the SDPs³⁰.

Descendent states with magnetism

Next, we discuss the topological phases that emerge when magnetism enters, which is natural in the system given that the Eu half-filled $4f$ orbital provide a large local magnetic moment^{25, 29, 37-39}. So far there has been no experimental studies on the magnetic ground state of EuTl_2 . In this work we consider the descendent phases originating from the development of commensurate A-type AFM orders (AFMA), i.e. ferromagnetic coupling within the Eu layer on the ab -plane and anti-ferromagnetic coupling along the stacking c -axis, as well as the FM order along the c -axis. From our DFT total energy calculations (see Table S1 in SI), although the FM order is preferred with the experimental structural parameters, after full relaxation in PBE+U+SOC, the AFM orders become more stable. For hexagonal Eu compounds, in contrast to the earlier reports of AFMA^{40,41}, recent experiment on EuCd_2As_2 found that the magnetic order can be manipulated by changing growth conditions to get either AFM or FM samples²⁹. We caution that incommensurate orders, like the helical order observed in EuIn_2As_2 ⁴², are also possible. The interplay between such incommensurate magnetic orders and the descendent topological phases from the multicritical parent is an interesting open question, but it is out of the scope of the present work.

For AFMA configuration, both time-reversal (T) and inversion (P) are broken. Additionally, for AFMA with moment along c -axis (AFMA c), the S_2 and M_y are broken, but the C_3 , M_z and G_x are retained. In contrast, for AFMA with moment along b -axis (AFMA b), the C_3 and M_z are removed, but the S_2 , M_y and G_x are retained. These changes of symmetry elements for different magnetic configurations will have consequences for the band structure and topological properties. We will show that the different topological characters are selectively tuned in the different magnetic configurations based on our understanding of the composite topological features in the parent TRS-protected EuTl_2 .

AFMAc Dirac semimetal: Although T and P are both broken in the AFMA configurations, the (TP) combination can still give Kramer pairs and band double degeneracy due to the anti-unitary $(TP)^2 = -1$. The bulk band structures of AFMAc in Fig.4(a) is similar to the nonmagnetic case with a BDP along Γ - A direction protected by C_3 , as shown in Fig.4(b). One difference is that the extra band degeneracy along the A - L direction on $k_z=\pi$ plane in the nonmagnetic is lifted in AFMAc for breaking the non-symmorphic S_2 . Turning to the surface state signature for this pair of AFM-BDP, there are four surface bands converging to the BDP projection on the (001) in Fig.4(e). The corresponding Fermi arcs are clearly shown in Fig.4(f) on the (100). In contrast, the SDPs at the three \bar{M} on (001) are all gapped out due to the breaking of both T and M_y , as shown in Fig.4(c). In contrast, M_z is still a good symmetry and the calculated M_z MCN changes from 2 to 1 on $k_z=0$ plane, while it remains as 0 on $k_z=\pi$ plane (see Fig.S3 in SI), implying the system could become an axion insulator if the BDPs could be gapped out by a small perturbation. On the (010) surface, there are still hourglass features, but the crossing is pushed from \bar{X} - \bar{S} to \bar{S} - \bar{Y} direction as seen in Fig.4(d). Comparing to the parent EuTl₂, the SDP features protected by M_y is selectively removed in AFMAc.

Around the BDP, the band inversion is between the bonding Tl p_x - p_y band and anti-bonding Tl p_z band with some Eu s character. For PM in space group (SG) 194, the irreducible representations are Γ_7^+ and Γ_9^+ for the two doubly degenerated bands, respectively, and a low-energy effective 4-band Hamiltonian similarly to BaAuBi⁴³ and Na₃Bi⁴⁴ can be constructed under T -invariant. In contrast, although the pair of BDPs in AFMAc is still protected by C_3 , the combined symmetry (TP) means the Hamiltonian for AFMAc should not be T -invariant anymore. For AFMAc, the magnetic space group (MSG) is 194.266. For the co-representations of this type-III MSG, the unitary SG is 190. We have used theory of invariant⁴⁵ to construct the 4-band $k \cdot p$ model by considering the Dirac Γ matrices and polynomials that are compatible under the symmetry transformations in MSG-194.266.

$$H(\mathbf{k}) = \varepsilon_0(\mathbf{k})\mathbb{I}_{4 \times 4} + M(\mathbf{k})\tau_z\sigma_0 + H_1(\mathbf{k}) + H_2(\mathbf{k}) \quad (1)$$

$$H_1(\mathbf{k}) = Bk_z\tau_y\sigma_0 + A(k_x\tau_x\sigma_y + k_y\tau_x\sigma_x) \quad (2)$$

$$H_2(\mathbf{k}) = D \left((k_x^2 - k_y^2)\tau_x\sigma_y + 2k_xk_y\tau_x\sigma_x \right) \quad (3)$$

where σ and τ are Pauli matrices for spin and orbital, respectively.

Among the different terms in $H(\mathbf{k})$, $H_2(\mathbf{k})$ breaks T , while the whole Hamiltonian is invariant under the combined symmetry (TP). After unitary transformation to make the coefficients of the matrix elements real, the Hamiltonian can be written as,

$$H(\mathbf{k}) = \varepsilon_0(\mathbf{k}) + \begin{pmatrix} M(\mathbf{k}) & Bk_z & 0 & Ak_+ + Dk_+^2 \\ Bk_z & -M(\mathbf{k}) & -Ak_+ - Dk_+^2 & 0 \\ 0 & -Ak_- - Dk_-^2 & M(\mathbf{k}) & Bk_z \\ Ak_- + Dk_-^2 & 0 & Bk_z & -M(\mathbf{k}) \end{pmatrix} \quad (4)$$

where $k_{\pm} = k_x \pm ik_y$, $M(\mathbf{k}) = M_0 - M_1k_z^2 - M_2(k_x^2 + k_y^2)$, and $\varepsilon_0(\mathbf{k}) = C_0 + C_1k_z^2 + C_2(k_x^2 + k_y^2)$. After diagonalization, the energy eigenvalues are

$$E(k) = \varepsilon_0(\mathbf{k}) \pm \sqrt{M(\mathbf{k})^2 + B^2k_z^2 + A^2(k_x^2 + k_y^2) + 2ADk_x(k_x^2 + k_y^2) + D^2(k_x^2 + k_y^2)^2} \quad (5)$$

When fitted to DFT calculated band structures, the following parameters are obtained, $C_0 = -0.081$ eV, $C_1 = -1.186$ eVÅ², $C_2 = 42.777$ eVÅ², $M_0 = 0.736$ eV, $M_1 = 5.429$ eVÅ², $M_2 = 32.573$ eVÅ², $A = 1.463$ eVÅ, $B = 0.000$ eVÅ and $D = 0.086$ eVÅ². The BDP in AFMAc has the momentum-energy of (0.0, 0.0, ± 0.37 Å⁻¹; $E_F - 0.25$ eV).

AFMAb Axion insulator: When the AFMA configuration has magnetic moments in-plane along b -axis (AFMAb) (Fig.5(a)), the C_3 and M_z are broken, while S_2 , M_y and G_x survive. The system still has the (TP) symmetry and the band double degeneracy. The band structure of AFMAb in Fig.5(a) shows that the BDP is gapped out due to the breaking of C_3 . In contrast to the gap due to strain resulting in a TCI with M_y MCN of 2 or 0, the WCC evolution in Fig.5(b) shows that M_y MCN is 1, thus the system becomes an axion insulator. This should be contrasted with the nonmagnetic strain-induced gapping, since in the that case T dictates that the MCN contribution coming from each of the BDPs is the same, and so the resulting MCNs are $1 \pm 1 = 0$ or 2. In contrast, the MCN contribution from the two BDPs cancel each other when going into the AFMAb phase, revealing the underlying M_y MCN=1, which one could have attempted to assign to the high-symmetry phase. As seen from Fig.5(c), only a single SDP survives in the vicinity of the \bar{M} point protected by M_y , among the four gapless SDPs on (001) in nonmagnetic EuTl₂. There is no SDP at the $\bar{\Gamma}$ point (see Fig.S4 in SI). On the (010) surface, the hourglass features in Fig.5(d) also give an odd number of surface band crossings, as is expected for an axion

insulator. Another notable feature is that the original Dirac point at the \bar{X} point is now moved slightly away towards to \bar{S} point.

FMc Weyl semimetal: Lastly, we consider the band structure of the FM configuration with moments along the c -axis (FM c). For FM c , T is broken, but P and the S_2 remain. There is no combined (TP) symmetry. As shown in Fig.6(a), with breaking T but preserving P , the band double degeneracy is all lifted except for along the high-symmetric A - L direction, which is protected by the S_2 . There are 14 pairs of Weyl points (WPs), which can be grouped into three sets of symmetry-related pairs, as shown in Fig.6(b). The momentum-energy of all WPs are also listed in Table S2. Set 1 has two pairs of WPs along the Γ - A direction by splitting the pair of BDP. Set 2 of six pairs of WPs are parallelly separated away from the $k_z=0$ plane, while the Set 3 of another six pairs of WPs are along the Γ - K direction on the $k_z=0$ plane. The Berry curvatures of the selected pairs of WPs in each set have been plotted in Fig.S5 to confirm their monopole features (see Fig.S5 in SI). For Set 1 with the two pairs of WPs split from the pair of BDP, one pair is at $E_F-0.18$ eV and the other at $E_F-0.24$ eV. When projected on (001), two sets of surface bands converging to the two sets of WPs separately at different energies in Fig.6(c), which can be compared to Fig.4(e) with all four surface bands converging to the same projected point for the BDP pair. Similarly, for the Fermi arcs in Fig.6(d) coming out from the WP projections on (100), comparing to the closed Fermi arcs in Fig.4(f) for the BDP pair, the arcs are split into two open pieces, giving the surface signature of WPs.

Conclusions

In conclusion, we have shown that EuTl₂ is a paradigmatic multicritical topological material enabling the access of a plethora of distinct topological phases by tuning strain and magnetic configurations. Remarkably, the phases realized include both Dirac and Weyl semimetals, the axion insulator, and a variety of other topological crystalline insulators protected by the combinations of different spatial symmetries. Correspondingly, the associated surface state signatures include surface Dirac points which may or may not be pinned to high-symmetry points, as well as hourglass fermions. Our calculations show that the relation between the surface dispersion and the bulk topological diagnosis could be rather subtle, and therefore caution must be used in viewing the surface states as a smoking-

gun signal of the topological phase realized. The prospect of using strain and magnetic field to drive phase transitions between different topological phases warrants further experimental investigations.

Acknowledgements

We thank Paul C. Canfield and Adam Kaminski for inspiring discussions. This work was supported as part of the Center for the Advancement of Topological Semimetals, an Energy Frontier Research Center funded by the U.S. Department of Energy Office of Science, Office of Basic Energy Sciences through the Ames Laboratory under its Contract No. DE-AC02-07CH11358. R.-J. S. in addition acknowledges funding via the Marie Skłodowska-Curie programme [EC Grant No. 842901] and the Winton programme as well as Trinity College at the University of Cambridge. The work of H.C.P. is supported by a Pappalardo Fellowship at MIT and a Croucher Foundation Fellowship.

Computational Methods

All density functional theory^{46, 47} (DFT) calculations with and without spin-orbit coupling (SOC) were performed with the PBE⁴⁸ exchange-correlation functional using a plane-wave basis set and projector augmented wave method⁴⁹, as implemented in the Vienna Ab-initio Simulation Package (VASP)^{50, 51}. Using maximally localized Wannier functions^{52, 53}, tight-binding models were constructed to reproduce closely the band structure including SOC within $E_F \pm 1$ eV with Eu *s-d-f* and Tl *s-p* orbitals. The surface Fermi arcs and spectral functions were calculated with the surface Green's function methods^{54, 55} as implemented in WannierTools⁵⁶. In the DFT calculations, we used a kinetic energy cutoff of 250 eV, Γ -centered Monkhorst-Pack⁵⁷ ($10 \times 10 \times 6$) *k*-point mesh, and a Gaussian smearing of 0.05 eV. To account for the strongly localized Eu 4*f* orbitals, an onsite Hubbard-like⁵⁸ $U=5.0$ eV is used. For band structure calculations of EuTl₂, we have used the experimental structural parameters⁵⁹, $a = 5.035$ Å, $c = 7.964$ Å with Eu at 2*b* positions of (0, 0, 1/4) and Tl at 4*f* positions of (1/3, 2/3, 0.044).

Competing Interests: The authors declare that there are no competing interests.

Author Contributions: L.-L.W., H.C.P., R.-J.S. and A. V. conceived and designed the project. L.-L.W. performed ab initio calculations. H.C.P., R.-J.S. and A. V. performed symmetry-based analysis. All authors contributed to the writing and editing of the manuscript.

Data Availability: The data that support the findings of this study are available in Materials Data Facility (hyperlink will appear later)

Table 1. Summary of symmetries and topological diagnosis of EuTiI_2 . The paramagnetic high-symmetry phase belongs to space group (SG) 194, and when either tensile or compressive strain is incorporated the spatial symmetries are reduced to those of SG 63. The ordering associated with the magnetic structures AFMAc , AFMAb and FMc are defined in the text, and we indicate their magnetic space groups (MSGs) in the Belov-Neronova-Smirnova notation. Asterisk (*) indicates the bulk is gapless. \times indicates the symmetry is broken, and 0 indicates the system does not possess a nontrivial topological index associated with the symmetry. For M_y and M_z , we indicate the computed mirror Chern number for the mirror plane containing the Γ point. For P , we indicate the Z_4 -valued symmetry indicator appropriate for the symmetry setting (paramagnetic vs. magnetic). For the rest of the symmetries, we indicate the Z_2 crystalline invariant one could infer from the invariants associated with M_y , M_z , and P . When the invariant is undetermined due to the gapless nature of the bulk we enter * in the corresponding entry. Note that, for the magnetic phases, a \times for an order-two symmetry G (all the symmetries below except for C_3) is synonymous with GT being a symmetry, where T denotes time-reversal. In particular, the axion insulator AFMAb also automatically realizes the nontrivial phase protected by the C_2T symmetry, and therefore could host hinge modes on suitable edges.

Structure & Sym.	C_3	M_y	M_z	P	G_x	C_{2y}	C_{2x}	S_2
Parent* (SG 194)	0	*	2	2	*	*	*	*
Tensile strain (SG 63)	\times	0	2	2	0	1	1	0
Compressive strain (SG 63)	\times	2	2	2	1	0	0	0
AFMAc^* (MSG 194.266)	0	\times	1	\times	*	*	\times	\times
AFMAb (MSG 63.461)	\times	1	\times	\times	1	\times	\times	0
FMc^* (MSG 194.270)	0	\times	*	0	\times	\times	\times	0

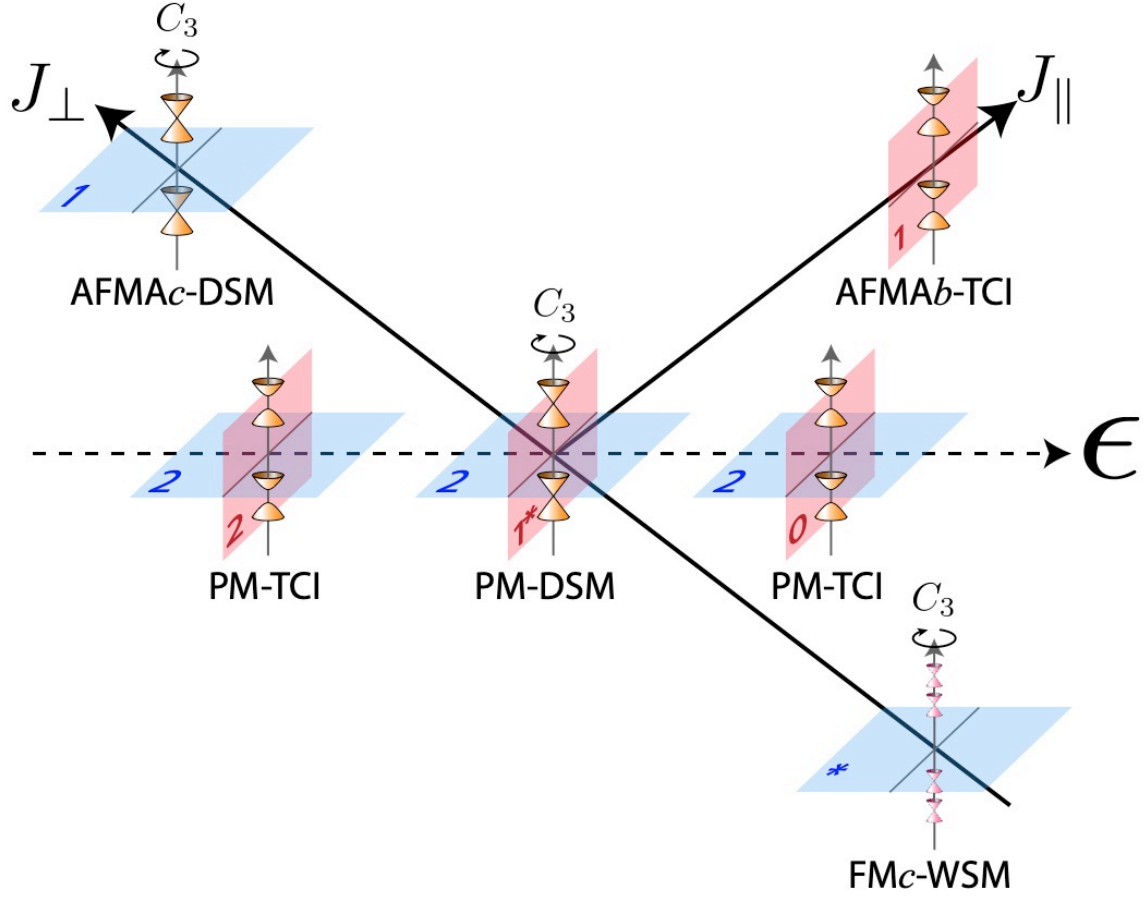


Figure 1. Different topological phases in EuTl_2 tuned by strain (ϵ) and interlayer (J_\perp) and intralayer (J_\parallel) magnetic couplings. The highest-symmetry paramagnetic (PM) Dirac semimetal in the middle serves as the parent phase and spawns a variety of descendent semi-metallic (SM) or topological crystalline insulator (TCI) phases when the symmetry is lowered. Dirac (D) and Weyl (W) cones are represented by orange and pink cones, respectively. Red and blue shades indicate mirror planes and the associated mirror Chern numbers are engraved. Asterisk (*) indicates the presence of gapless points on the planes, which render the invariants ill-defined. Both A-type antiferromagnetic (AFMA) and ferromagnetic (FM) magnetic structures are considered, with the last character denoting the crystalline axis along which the magnetic moments point. Note that for FM c -WSM there are additional Weyl points, some residing on and near the blue mirror plane, which are not shown for simplicity.

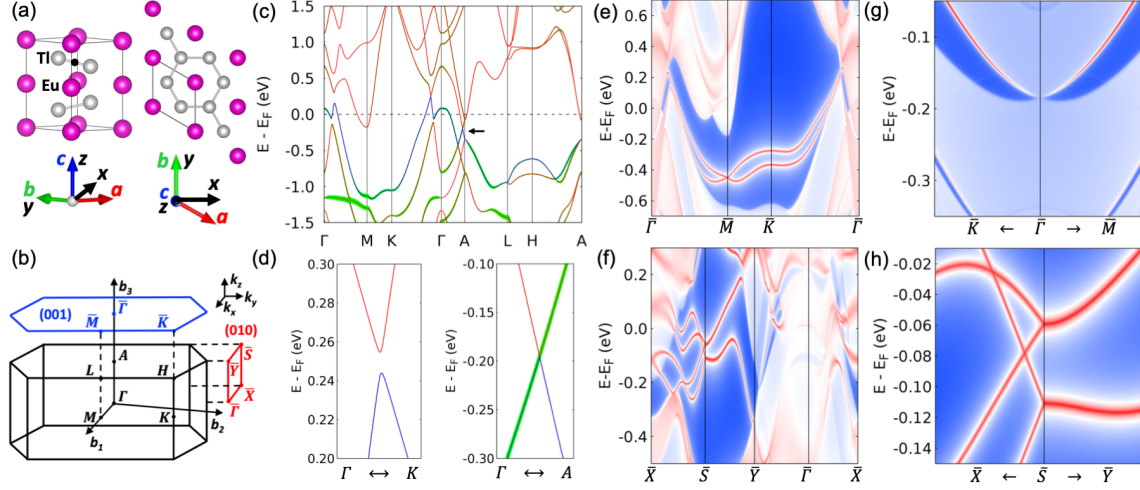


Figure 2. (a) Crystal structure of EuTl_2 in space group 194 ($P6_3/mmc$) in both side view and top view. Eu (Tl) atoms are magenta (gray) spheres. The inversion center at mid-point of Tl-Tl bond in the buckled honeycomb layer is marked by a black circle. (b) 3D bulk Brillouin zone (BZ) of EuTl_2 and 2D surface Brillouin zone (SBZ) on (001) and (010) with high-symmetry points labeled. (c) Bulk band structure of nonmagnetic EuTl_2 in PBE+SOC without $4f$ orbitals and (d) zoomed along Γ - K and Γ - A directions. The top valence band is in blue and the green shade stands for the projection of Tl p_y orbitals. Black arrow points to the bulk Dirac points along Γ - A . Panel (e) and (f) are surface states of (001) and (010) with features zoomed in (g) and (h), respectively. Blue, white and red colors stand for low, medium, and high density of states.

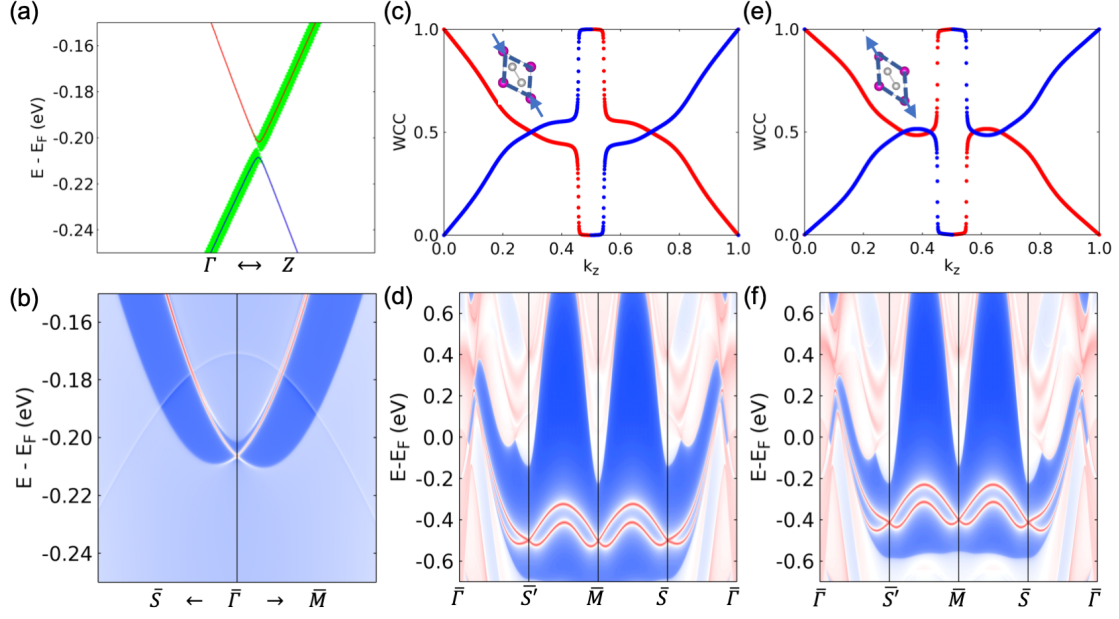


Figure 3. (a) Bulk band structure of nonmagnetic EuTl₂ with -2% strain zoomed along Γ -Z direction in the base-centered orthorhombic structure (space group 63) showing the bulk gap opening. The valence band is in blue and the green shade stands for the projection of Tl p_y orbitals. (b) (001) surface states zoomed along \bar{S} - $\bar{\Gamma}$ - \bar{M} direction showing the surface Dirac point at $\bar{\Gamma}$ with -2% strain. Panel (c) and (e) are the Wannier charge center (WCC) evolution for calculating the M_y mirror Chern number (MCN) of 2 and 0 at -2% and +2% strain, respectively. Panel (d) and (f) are the (001) surface states at -2% and +2% strain, respectively, in the base-centered orthorhombic structure. Note that the surface band structures are essentially insensitive to the different bulk topologies.

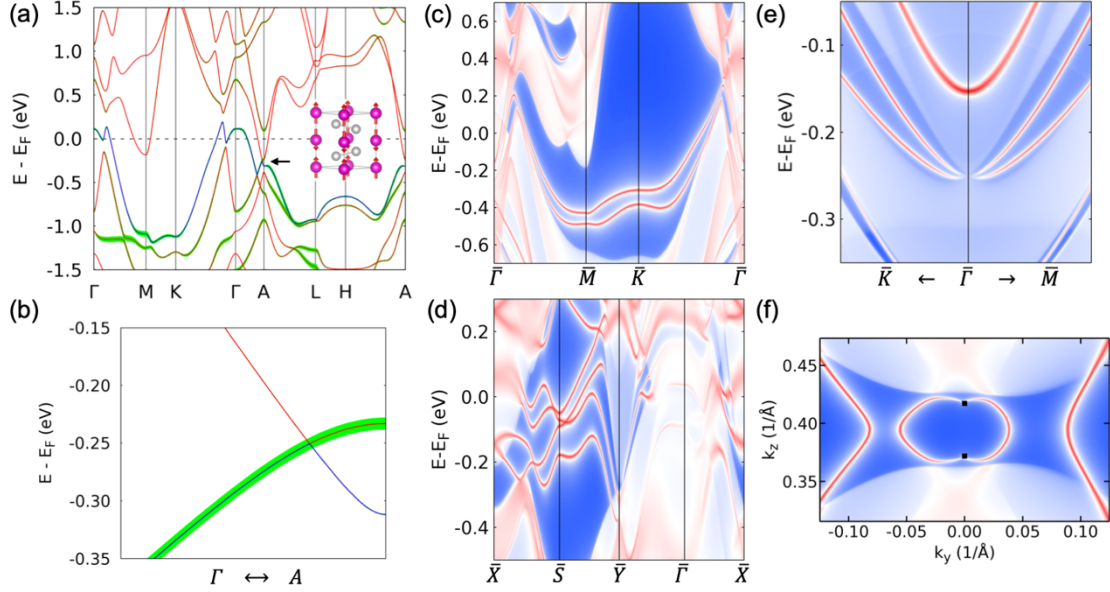


Figure 4. (a) Bulk band structure of EuTl_2 in PBE+SOC+U for A-type AFM with moment along c -axis (AFMA c). The inset shows the magnetic configuration. Black arrow points the bulk Dirac point and zoomed along Γ - A direction in (b). The valence band is in blue and the green shade stands for the projection of Tl p_y orbitals. Panel (c) and (d) are the surface states on (001) and (010), respectively. (e) Surface states zoomed around $\bar{\Gamma}$ point on (001) (f) 2D Fermi surface (FS) on (100) at $E_F - 0.25$ eV. The projections of the bulk Dirac points are labeled by black squares.

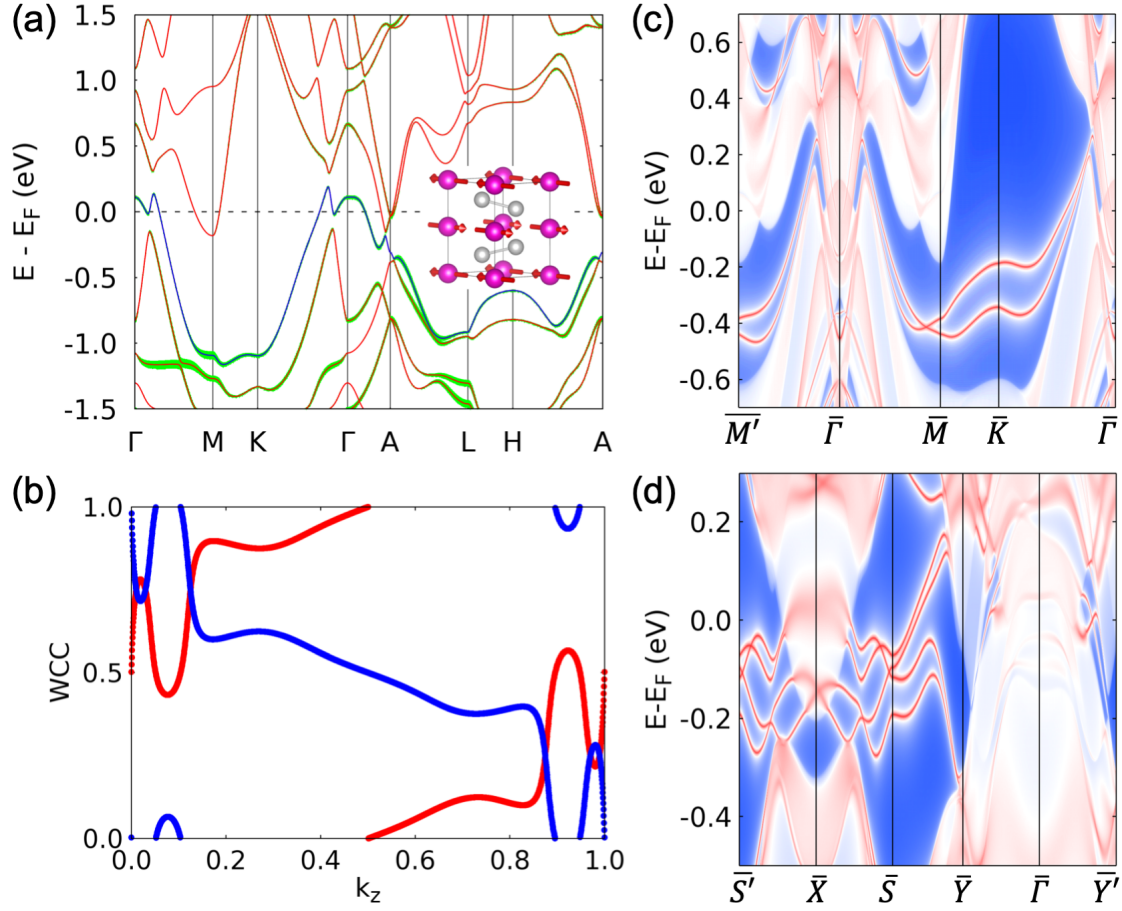


Figure 5. (a) Bulk band structure of EuTl₂ in PBE+SOC+U for A-type AFM with moment along *b*-axis (AFMA*b*). The inset shows the magnetic configuration. The valence band is in blue and the green shade stands for the projection of Tl *p_y* orbitals. (b) WCC evolution of mirror eigenvalue of $+i$ (red) and $-i$ (blue) giving the M_y MCN of 1. Panel (c) and (d) are the surface states on (001) and (010), respectively.

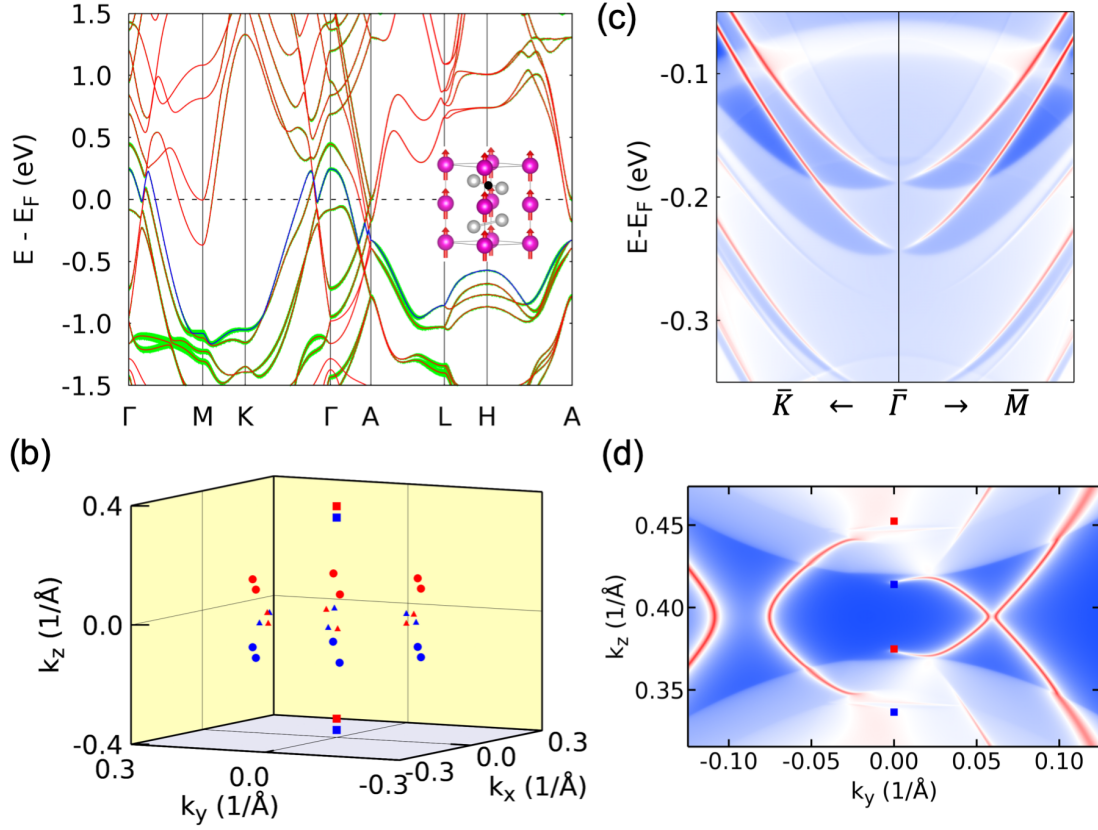


Figure 6. (a) Bulk band structure of EuTl₂ in PBE+SOC+U for FM with moment along *c*-axis (FMc). (b) Three sets of Weyl points (WPs) including two pairs along k_z (squares) split from bulk Dirac points, six pairs parallelly separated across $k_z=0$ plane (circles) and six pairs on $k_z=0$ plane (triangles). Red (blue) stands for the chirality of +1 (-1). (c) The surface states on (001) around $\bar{\Gamma}$ point showing the two WPs split from the DP at $E_F-0.25$ eV and (d) the corresponding open Fermi arcs projected on the side (100) surface. The projections of the first set of WPs are labeled by red and blue squares.

References

1. M. Z. Hasan, C. L. Kane, Colloquium: Topological insulators. *Rev Mod Phys* **82**, 3045 (2010).
2. X.-L. Qi, S.-C. Zhang, Topological insulators and superconductors. *Rev Mod Phys* **83**, 1057-1110 (2011).
3. A. Bansil, H. Lin, T. Das, Colloquium: Topological band theory. *Rev Mod Phys* **88**, 021004 (2016).
4. N. P. Armitage, E. J. Mele, A. Vishwanath, Weyl and Dirac semimetals in three-dimensional solids. *Rev Mod Phys* **90**, 015001 (2018).
5. H. C. Po, A. Vishwanath, H. Watanabe, Symmetry-based indicators of band topology in the 230 space groups (vol 8, 50, 2017). *Nat Commun* **8**, 50 (2017).
6. R. J. Slager, A. Mesaros, V. Juricic, J. Zaanen, The space group classification of topological band-insulators. *Nat Phys* **9**, 98-102 (2013).
7. J. Kruthoff, J. de Boer, J. van Wezel, C. L. Kane, R.-J. Slager, Topological Classification of Crystalline Insulators through Band Structure Combinatorics. *Phys Rev X* **7**, 041069 (2017).
8. B. Bradlyn, L. Elcoro, J. Cano, M. G. Vergniory, Z. J. Wang, C. Felser, M. I. Aroyo, B. A. Bernevig, Topological quantum chemistry. *Nature* **547**, 298-305 (2017).
9. E. Khalaf, H. C. Po, A. Vishwanath, H. Watanabe, Symmetry Indicators and Anomalous Surface States of Topological Crystalline Insulators. *Phys Rev X* **8**, 031070 (2018).
10. Z. D. Song, T. T. Zhang, Z. Fang, C. Fang, Quantitative mappings between symmetry and topology in solids. *Nat Commun* **9**, 3530 (2018).
11. F. Tang, H. C. Po, A. Vishwanath, X. G. Wan, Comprehensive search for topological materials using symmetry indicators. *Nature* **566**, 486-490 (2019).
12. M. G. Vergniory, L. Elcoro, C. Felser, N. Regnault, B. A. Bernevig, Z. J. Wang, A complete catalogue of high-quality topological materials. *Nature* **566**, 480-485 (2019).
13. T. T. Zhang, Y. Jiang, Z. D. Song, H. Huang, Y. Q. He, Z. Fang, H. M. Weng, C. Fang, Catalogue of topological electronic materials. *Nature* **566**, 475-479 (2019).
14. H. Watanabe, H. C. Po, A. Vishwanath, Structure and topology of band structures in the 1651 magnetic space groups. *Science Advances* **4**, eaat8685 (2018).
15. R. S. K. Mong, A. M. Essin, J. E. Moore, Antiferromagnetic topological insulators. *Phys Rev B* **81**, 245209 (2010).
16. A. M. Turner, Y. Zhang, R. S. K. Mong, A. Vishwanath, Quantized response and topology of magnetic insulators with inversion symmetry. *Phys Rev B* **85**, 165120 (2012).

17. N. Varnava, D. Vanderbilt, Surfaces of axion insulators. *Phys Rev B* **98**, 245117 (2018).
18. M. M. Otrokov, I. I. Klimovskikh, H. Bentmann, D. Estyunin, A. Zeugner, Z. S. Aliev, S. Gaß, A. U. B. Wolter, A. V. Koroleva, A. M. Shikin, M. Blanco-Rey, M. Hoffmann, I. P. Rusinov, A. Y. Vyazovskaya, S. V. Eremeev, Y. M. Koroteev, V. M. Kuznetsov, F. Freyse, J. Sánchez-Barriga, I. R. Amiraslanov, M. B. Babanly, N. T. Mamedov, N. A. Abdullayev, V. N. Zverev, A. Alfonsov, V. Kataev, B. Büchner, E. F. Schwier, S. Kumar, A. Kimura, L. Petaccia, G. Di Santo, R. C. Vidal, S. Schatz, K. Kißner, M. Ünzelmann, C. H. Min, S. Moser, T. R. F. Peixoto, F. Reinert, A. Ernst, P. M. Echenique, A. Isaeva, E. V. Chulkov, Prediction and observation of an antiferromagnetic topological insulator. *Nature* **576**, 416-422 (2019).
19. D. Zhang, M. Shi, T. Zhu, D. Xing, H. Zhang, J. Wang, Topological Axion States in the Magnetic Insulator MnBi_2Te_4 with the Quantized Magnetoelectric Effect. *Phys Rev Lett* **122**, 206401 (2019).
20. P. Swatek, Y. Wu, L.-L. Wang, K. Lee, B. Schruk, J. Yan, A. Kaminski, Gapless Dirac surface states in the antiferromagnetic topological insulator MnBi_2Te_4 . *Phys Rev B* **101**, 161109 (2020).
21. N. H. Jo, L.-L. Wang, R.-J. Slager, J. Yan, Y. Wu, K. Lee, B. Schruk, A. Vishwanath, A. Kaminski, Intrinsic axion insulating behavior in antiferromagnetic $\text{MnBi}_6\text{Te}_{10}$. *Phys Rev B* **102**, 045130 (2020).
22. Y.-J. Hao, P. Liu, Y. Feng, X.-M. Ma, E. F. Schwier, M. Arita, S. Kumar, C. Hu, R. e. Lu, M. Zeng, Y. Wang, Z. Hao, H.-Y. Sun, K. Zhang, J. Mei, N. Ni, L. Wu, K. Shimada, C. Chen, Q. Liu, C. Liu, Gapless Surface Dirac Cone in Antiferromagnetic Topological Insulator MnBi_2Te_4 . *Phys Rev X* **9**, 041038 (2019).
23. Y. J. Chen, L. X. Xu, J. H. Li, Y. W. Li, H. Y. Wang, C. F. Zhang, H. Li, Y. Wu, A. J. Liang, C. Chen, S. W. Jung, C. Cacho, Y. H. Mao, S. Liu, M. X. Wang, Y. F. Guo, Y. Xu, Z. K. Liu, L. X. Yang, Y. L. Chen, Topological Electronic Structure and Its Temperature Evolution in Antiferromagnetic Topological Insulator MnBi_2Te_4 . *Phys Rev X* **9**, 041040 (2019).
24. H. Li, S.-Y. Gao, S.-F. Duan, Y.-F. Xu, K.-J. Zhu, S.-J. Tian, J.-C. Gao, W.-H. Fan, Z.-C. Rao, J.-R. Huang, J.-J. Li, D.-Y. Yan, Z.-T. Liu, W.-L. Liu, Y.-B. Huang, Y.-L. Li, Y. Liu, G.-B. Zhang, P. Zhang, T. Kondo, S. Shin, H.-C. Lei, Y.-G. Shi, W.-T. Zhang, H.-M. Weng, T. Qian, H. Ding, Dirac Surface States in Intrinsic Magnetic Topological Insulators EuSn_2As_2 and $\text{MnBi}_{2n}\text{Te}_{3n+1}$. *Phys Rev X* **9**, 041039 (2019).
25. Y. F. Xu, Z. D. Song, Z. J. Wang, H. M. Weng, X. Dai, Higher-Order Topology of the Axion Insulator EuIn_2As_2 . *Phys Rev Lett* **122**, 256402 (2019).
26. F. D. M. Haldane, Model for a Quantum Hall-Effect without Landau-Levels - Condensed-Matter Realization of the Parity Anomaly. *Phys Rev Lett* **61**, 2015-2018 (1988).

27. C. Z. Chang, J. S. Zhang, X. Feng, J. Shen, Z. C. Zhang, M. H. Guo, K. Li, Y. B. Ou, P. Wei, L. L. Wang, Z. Q. Ji, Y. Feng, S. H. Ji, X. Chen, J. F. Jia, X. Dai, Z. Fang, S. C. Zhang, K. He, Y. Y. Wang, L. Lu, X. C. Ma, Q. K. Xue, Experimental Observation of the Quantum Anomalous Hall Effect in a Magnetic Topological Insulator. *Science* **340**, 167-170 (2013).
28. B. J. Wieder, Y. Kim, A. M. Rappe, C. L. Kane, Double Dirac Semimetals in Three Dimensions. *Phys Rev Lett* **116**, 186402 (2016).
29. N. H. Jo, B. Kuthanazhi, Y. Wu, E. Timmons, T.-H. Kim, L. Zhou, L.-L. Wang, B. G. Ueland, A. Palasyuk, D. H. Ryan, R. J. McQueeney, K. Lee, B. Schruck, A. A. Burkov, R. Prozorov, S. L. Bud'ko, A. Kaminski, P. C. Canfield, Manipulating magnetism in the topological semimetal EuCd₂As₂. *Phys Rev B* **101**, 140402 (2020).
30. T. H. Hsieh, H. Lin, J. W. Liu, W. H. Duan, A. Bansil, L. Fu, Topological crystalline insulators in the SnTe material class. *Nat Commun* **3**, 982 (2012).
31. L. A. Fu, Topological Crystalline Insulators. *Phys Rev Lett* **106**, 106802 (2011).
32. Z. J. Wang, A. Alexandradinata, R. J. Cava, B. A. Bernevig, Hourglass fermions. *Nature* **532**, 189-194 (2016).
33. T. Zhang, Z. Cui, Z. Wang, H. Weng, Z. Fang, BaHgSn: A Dirac semimetal with surface hourglass fermions. *Phys Rev B* **101**, 115145 (2020).
34. Z. Zhu, Z.-M. Yu, W. Wu, L. Zhang, W. Zhang, F. Zhang, S. A. Yang, Composite Dirac semimetals. *Phys Rev B* **100**, 161401 (2019).
35. Z. Song, S.-J. Huang, Y. Qi, C. Fang, M. Hermele, Topological states from topological crystals. *Science Advances* **5**, eaax2007 (2019).
36. A. Bouhon, A. M. Black-Schaffer, R.-J. Slager, Wilson loop approach to fragile topology of split elementary band representations and topological crystalline insulators with time-reversal symmetry. *Phys Rev B* **100**, 195135 (2019).
37. G. Hua, S. Nie, Z. Song, R. Yu, G. Xu, K. Yao, Dirac semimetal in type-IV magnetic space groups. *Phys Rev B* **98**, 201116 (2018).
38. L. L. Wang, N. H. Jo, B. Kuthanazhi, Y. Wu, R. J. McQueeney, A. Kaminski, P. C. Canfield, Single pair of Weyl fermions in the half-metallic semimetal EuCd₂As₂. *Phys Rev B* **99**, 245147 (2019).
39. J. R. Soh, F. de Juan, M. G. Vergniory, N. B. M. Schröter, M. C. Rahn, D. Y. Yan, J. Jiang, M. Bristow, P. Reiss, J. N. Blandy, Y. F. Guo, Y. G. Shi, T. K. Kim, A. McCollam, S. H. Simon, Y. Chen, A. I. Coldea, A. T. Boothroyd, Ideal Weyl semimetal induced by magnetic exchange. *Phys Rev B* **100**, 201102 (2019).
40. M. C. Rahn, J. R. Soh, S. Francoual, L. S. I. Veiga, J. Stremper, J. Mardegan, D. Y. Yan, Y. F. Guo, Y. G. Shi, A. T. Boothroyd, Coupling of magnetic order and charge transport in the candidate Dirac semimetal EuCd₂As₂. *Phys Rev B* **97**, 214422 (2018).

41. S. Pakhira, T. Heitmann, S. X. M. Riberolles, B. G. Ueland, R. J. McQueeney, D. C. Johnston, D. Vaknin, Zero-field magnetic ground state of EuMg_2Bi_2 . *Phys Rev B* **103**, 024408 (2021).
42. S. X. M. Riberolles, T. V. Trevisan, B. Kuthanazhi, T. W. Heitmann, F. Ye, D. C. Johnston, S. L. Bud'ko, D. H. Ryan, P. C. Canfield, A. Kreyssig, A. Vishwanath, R. J. McQueeney, L. L. Wang, P. P. Orth, B. G. Ueland, Magnetic crystalline-symmetry-protected axion electrodynamics and field-tunable unpinned Dirac cones in EuIn_2As_2 . *Nat Commun* **12**, 999 (2021).
43. Y. P. Du, B. Wan, D. Wang, L. Sheng, C. G. Duan, X. G. Wan, Dirac and Weyl Semimetal in XYBi ($\text{X} = \text{Ba, Eu}$; $\text{Y} = \text{Cu, Ag and Au}$). *Sci Rep-Uk* **5**, 14423 (2015).
44. Z. J. Wang, Y. Sun, X. Q. Chen, C. Franchini, G. Xu, H. M. Weng, X. Dai, Z. Fang, Dirac semimetal and topological phase transitions in A(3)Bi ($\text{A} = \text{Na, K, Rb}$). *Phys Rev B* **85**, 195320 (2012).
45. C.-X. Liu, X.-L. Qi, H. Zhang, X. Dai, Z. Fang, S.-C. Zhang, Model Hamiltonian for topological insulators. *Phys Rev B* **82**, 045122 (2010).
46. P. Hohenberg, W. Kohn, Inhomogeneous Electron Gas. *Phys. Rev.* **136**, B864-B871 (1964).
47. W. Kohn, L. J. Sham, Self-Consistent Equations Including Exchange and Correlation Effects. *Phys. Rev.* **140**, A1133-A1138 (1965).
48. J. P. Perdew, K. Burke, M. Ernzerhof, Generalized gradient approximation made simple. *Phys Rev Lett* **77**, 3865-3868 (1996).
49. P. E. Blöchl, Projector Augmented-Wave Method. *Phys Rev B* **50**, 17953-17979 (1994).
50. G. Kresse, J. Furthmüller, Efficient Iterative Schemes for Ab initio Total-Energy Calculations Using a Plane-Wave Basis Set. *Phys Rev B* **54**, 11169-11186 (1996).
51. G. Kresse, J. Furthmüller, Efficiency of Ab-initio Total Energy Calculations for Metals and Semiconductors Using a Plane-Wave Basis Set. *Comp Mater Sci* **6**, 15-50 (1996).
52. N. Marzari, D. Vanderbilt, Maximally localized generalized Wannier functions for composite energy bands. *Phys Rev B* **56**, 12847-12865 (1997).
53. I. Souza, N. Marzari, D. Vanderbilt, Maximally localized Wannier functions for entangled energy bands. *Phys Rev B* **65**, 035109 (2001).
54. M. P. L. Sancho, J. M. L. Sancho, J. Rubio, Quick Iterative Scheme for the Calculation of Transfer-Matrices - Application to Mo(100) . *J Phys F Met Phys* **14**, 1205-1215 (1984).
55. M. P. L. Sancho, J. M. L. Sancho, J. Rubio, Highly Convergent Schemes for the Calculation of Bulk and Surface Green-Functions. *J Phys F Met Phys* **15**, 851-858 (1985).

- 56. Q. Wu, S. Zhang, H.-F. Song, M. Troyer, A. A. Soluyanov, WannierTools: An open-source software package for novel topological materials. *Computer Physics Communications* **224**, 405-416 (2018).
- 57. H. J. Monkhorst, J. D. Pack, Special Points for Brillouin-Zone Integrations. *Phys Rev B* **13**, 5188-5192 (1976).
- 58. S. L. Dudarev, G. A. Botton, S. Y. Savrasov, C. J. Humphreys, A. P. Sutton, Electron-energy-loss spectra and the structural stability of nickel oxide: An LSDA+U study. *Phys Rev B* **57**, 1505-1509 (1998).
- 59. A. Iandelli, MX₂-Verbindungen der Erdalkali- und Seltenen Erdmetalle mit Gallium, Indium und Thallium. *Z Anorg Allg Chem* **330**, 221-232 (1964).